NeuroImage: Clinical 7 (2015) 142–154

Contents lists available at ScienceDirect

NeuroImage: Clinical

journal homepage: www.elsevier.com/locate/ynicl

Mathematical models for the diffusion magnetic resonance signal abnormality in patients with prion diseases

Matteo Figini[a,b], Daniel C. Alexander[c], Veronica Redaelli[d], Fabrizio Fasano[e], Marina Grisoli[a], Giuseppe Baselli[b], Pierluigi Gambetti[f], Fabrizio Tagliavini[d], Alberto Bizzi[g,*]

[a] Neuroradiology, Fondazione IRCCS Istituto Neurologico "Carlo Besta", Milano, Italy
[b] Dipartimento di Elettronica, Informazione e Bioingegneria, Politecnico di Milano, Milano, Italy
[c] Centre for Medical Image Computing, Department of Computer Science, University College London, London, United Kingdom
[d] Neuropathology, Fondazione IRCCS Istituto Neurologico, Parma, Italy
[e] Department of Neuroscience, Università degli Studi di Parma, Parma, Italy
[f] National Prion Disease Pathology Surveillance Center, Department of Pathology, Case Western Reserve University, Cleveland, OH, USA
[g] Neuroradiology, Humanitas Research Hospital IRCCS, Rozzano, Milano, Italy

ARTICLE INFO

Article history:
Received 5 July 2014
Received in revised form 26 October 2014
Accepted 23 November 2014
Available online 29 November 2014

Keywords:
Diffusion MRI
Biophysical models
Creutzfeldt–Jakob disease
Prion disease
Spongiform degeneration

ABSTRACT

In clinical practice signal hyperintensity in the cortex and/or in the striatum on magnetic resonance (MR) diffusion-weighted images (DWIs) is a marker of sporadic Creutzfeldt–Jakob Disease (sCJD). MR diagnostic accuracy is greater than 90%, but the biophysical mechanisms underpinning the signal abnormality are unknown. The aim of this prospective study is to combine an advanced DWI protocol with new mathematical models of the microstructural changes occurring in prion disease patients to investigate the cause of MR signal alterations. This underpins the later development of more sensitive and specific image-based biomarkers. DWI data with a wide a range of echo times and diffusion weightings were acquired in 15 patients with suspected diagnosis of prion disease and in 4 healthy age-matched subjects. Clinical diagnosis of sCJD was made in nine patients, genetic CJD in one, rapidly progressive encephalopathy in three, and Gerstmann–Sträussler–Scheinker syndrome in two. Data were analysed with two bi-compartment models that represent different hypotheses about the histopathological alterations responsible for the DWI signal hyperintensity. A ROI-based analysis was performed in 13 grey matter areas located in affected and apparently unaffected regions from patients and healthy subjects. We provide for the first time non-invasive estimate of the restricted compartment radius, designed to reflect vacuole size, which is a key discriminator of sCJD subtypes. The estimated vacuole size in DWI hyperintense cortex was in the range between 3 and 10 μm that is compatible with neuropathology measurements. In DWI hyperintense grey matter of sCJD patients the two bi-compartment models outperform the classic mono-exponential ADC model. Both new models show that T_2 relaxation times significantly increase, fast and slow diffusivities reduce, and the fraction of the compartment with slow/restricted diffusion increases compared to unaffected grey matter of patients and healthy subjects. Analysis of the raw DWI signal allows us to suggest the following acquisition parameters for optimized detection of CJD lesions: $b = 3000$ s/mm^2 and TE = 103 ms. In conclusion, these results provide the first in vivo estimate of mean vacuole size, new insight on the mechanisms of DWI signal changes in prionopathies and open the way to designing an optimized acquisition protocol to improve early clinical diagnosis and subtyping of sCJD.

1. Introduction

Prion diseases are transmissible, rapidly progressive and fatal neurological diseases. Despite their rarity and the lack of an effective treatment, prion diseases draw exceptional scientific interest, mainly because of their peculiar transmission mechanism, involving the presence of a misfolded isoform (PrP^{Sc}) of the cellular prion protein (PrP^{C}) and unique histological lesions. Sporadic Creutzfeldt–Jakob disease (sCJD), the most common human prion disease, has a wide spectrum of clinical and histopathological phenotypic heterogeneity that has

Abbreviations: ADC, apparent diffusion coefficient; BIC, Bayesian information criterion; CJD, Creutzfeldt–Jakob disease; CNR, contrast to noise ratio; DWI, diffusion weighted imaging; EEG, electroencephalogram; EPI, echo-planar imaging; FOV, field of view; GSS, Gerstmann–Sträussler–Scheinker syndrome; MPRAGE, magnetization-prepared rapid acquisition gradient-echo; PrP^{C}, prion protein cellular; PrP^{Sc}, prion protein scrapie; ROI, region of interest; RPE, rapidly progressive encephalopathy; sCJD, sporadic Creutzfeldt–Jakob disease; SS-SE, single shot spin-echo; TE, echo time; TI, inversion time; TR, repetition time

* Corresponding author at: Neuroradiology, Humanitas Research Hospital IRCCS, Via Manzoni, 56, Rozzano, Milano 20089, Italy. Tel: +39 02 82246663.
E-mail address: alberto.bizzi@humanitas.it (A. Bizzi).

http://dx.doi.org/10.1016/j.nicl.2014.11.017

made its clinical recognition difficult. Four main neuropathological features of sCJD have been described: astrocytosis, neuronal loss, intracellular spongiform degeneration and PrP^{Sc} accumulation in extracellular space (Puoti et al., 2012). A great variability on lesion distribution, spongiform degeneration and PrP^{Sc} accumulation is influenced by the genotype at codon 129 and the PrP^{Sc} type (Gambetti et al., 2003). In particular, fine spongiosis with small vacuoles is characteristic of the most common phenotypes (MM1, MV1 and VV2), whereas coarse spongiosis with large vacuoles is found in the MM2C and MV2C subtypes (Parchi et al., 2012). For example, the vacuole average diameter in sCJDMM1 is 5.8 ± 1 μm, while in sCJDMM2, an sCJD subtype which can be difficult to distinguish clinically from sCJDMM1, the average vacuole diameter is larger than 15 μm. The subtypes have quite different prognosis (Gambetti et al., 2011), so a non-invasive technique for the estimation of vacuole size would have a great importance. However, currently, definite diagnosis of sCJD and its subtypes can be made only by brain tissue examination. Clinical criteria for the diagnosis of probable sCJD require the presence of at least two clinical signs out of (i) dementia, (ii) cerebellar or visual, (iii) pyramidal or extrapyramidal, (iv) akinetic mutism, and at least one of three tests 14-3-3 protein in CSF, periodic sharp-wave complexes in the EEG, or abnormally high signal on Magnetic Resonance Imaging (MRI) must be positive (Zerr et al., 2009). In particular, asymmetric MRI hyperintensities on diffusion-weighted images (DWIs) and T_2-weighted Fluid Attenuated Inversion Recovery (FLAIR) in at least three non-contiguous gyri or in the striatum or both are highly suggestive for the diagnosis of sCJD. DWI is the best among standard MRI sequences (Young et al., 2005; Kallenberg et al., 2006; Galanaud et al., 2010; Vitali et al., 2011) with a diagnostic accuracy above 90% (Shiga et al., 2004; Young et al., 2005; Satoh et al., 2007; Bizzi et al., 2009; Galanaud et al., 2010; Vitali et al., 2011). However, even though DWI hyperintensity is currently used as a marker of prion disease (Puoti et al., 2012), the tissue alteration underlying this imaging signal remains unknown. It has been reported that DWI sensitivity may vary among prion diseases and sCJD subtypes (Krasnianski et al., 2006), which opens the possibility to use it for early diagnosis of sCJD subtypes. Therefore, the identification of the histopathologic substrate associated with the DWI signal abnormality is important, because it can guide the precise choice of MRI protocol to maximize diagnostic power.

A few authors have looked for a correlation between neuropathological changes and DWI hyperintensity or reduction in apparent diffusion coefficient (ADC). According to some groups (Geschwind et al., 2009; Manners et al., 2009) DWI hyperintensities may be correlated with spongiosis and PrP^{Sc} deposition rather than with gliosis and neuronal loss; Lodi et al. (2009) found that patients with fatal insomnia, a prionopathy associated with little or no spongiform changes (Parchi et al., 1999), did not exhibit hyperintensities on DWI thus pointing to spongiosis as the principal determinant of DWI signal hyperintensity. On the other hand, Russmann et al. (2005) found no significant correlation between ADC and the degree of spongiosis, gliosis or neuronal loss.

The sensitivity of DWI to the random displacements of water molecules in biological tissues makes it useful as a probe of tissue microstructure. Previous MRI studies of prion disease have focused (qualitatively or semi-quantitatively) on the apparent hyperintensity on T_2-weighted FLAIR and DWI, or quantitatively on the ADC (Demaerel et al., 2003; Tschampa et al., 2003; Lin et al., 2006; Galanaud et al., 2008; Hyare et al., 2010a, b). Only a recent study (Caverzasi et al., 2014) performed a slightly more sophisticated analysis, by evaluating the fractional anisotropy (which did not show significant differences between patients and controls) and characterizing the evolution of ADC with the pathology progression, which revealed a non-linear trend.

Signal in DWI depends on several parameters (Mori and Barker, 1999), including T_2 relaxation (between 80 and 120 ms in healthy brain tissue, but tends to increase with structural damage), the proton density M_0, and the water mobility within the tissue. The ADC factors out T_2 and M_0 providing a purer index of water mobility, but is still influenced by a wide range of factors. Recent trends in DWI, so-called microstructure imaging, use mathematical models to relate DWI signals to histological features; see for example Assaf et al. (2004), Barazany et al. (2009), Panagiotaki et al. (2012), and Zhang et al. (2012). However, current techniques largely consider healthy white matter tissue, so are not directly applicable to explain the grey-matter DWI hyperintensity in prion disease.

In this prospective study we examine, for the first time in consecutive patients with suspected prion disease, the potential of more sophisticated mathematical models than the simple mono-exponential model used for ADC estimation. We develop a modelling approach based on two main hypotheses on the microstructural tissue alterations that may cause DWI hyperintensity. Each hypothesis leads to a different family of mathematical models for how the DWI signal varies with echo time TE, b-value and diffusion time. Our two hypotheses are: a) reduction of hindered diffusivity caused by prion PrP^{Sc} deposition in the extracellular space; and b) restriction of water diffusing within intracellular vacuoles. The key difference between the two hypotheses is that (b) implies restricted diffusion, whereas (a) does not. In normal grey matter, a single or bi-exponential model explains the DWI signal well (Clark and Le Bihan, 2000; Kiselev and Il'yasov, 2007). For hypothesis (a), we suppose that PrP^{Sc} deposition hinders diffusion (i.e. slows down but does not trap water molecules) in the extra-cellular space: the diffusivity is reduced in the lesions but the displacement distribution is still Gaussian with a variance linearly increasing with time. Thus we use a biexponential model (Niendorf et al., 1996; Clark and Le Bihan, 2000; Mulkern et al., 2001) to represent hypothesis (a). Under hypothesis (b), the confinement of water molecules inside the vacuoles leads to restricted diffusion that has a non-Gaussian displacement distribution that depends on the average size of the vacuoles. This condition is modelled with a two-compartment model, with restricted diffusion in a spherical compartment (the vacuoles) and hindered diffusion in the other compartment, corresponding to the extracellular space in the voxel. Each more provides estimates of various parameters that contain more specific information than the ADC. Both estimate compartmental diffusivities, as well as volume fractions for each compartment. Moreover, model (b) provides estimates of the average vacuole size, which offers potential as a non-invasive biomarker that discriminates prion disease subtypes. We also tested the standard mono-exponential model (the ADC) for comparison with both of the newly proposed models.

To test and compare the different mathematical models, we designed an advanced acquisition scheme that explores the possible range of different diffusion-weightings (b-values), diffusion times and T_2-weightings as widely as possible on a clinical 1.5 Tesla MR scanner. The scheme provides a uniquely broad sampling of the possible space of measurements with which to evaluate the candidate models. The acquisition is not intended as practical to run routinely for clinical assessment, but rather to provide the best information with which to identify an appropriate model. Once we have such a model, we can use it to find an economical imaging scheme that is practical for clinical assessment, for example using the experiment design optimization algorithm described by Alexander (2008).

Overall, the study has two main aims: i) to evaluate the MR parameters of each model in healthy subjects and patients in order to see which are informative about the presence of prion pathology and to understand if the proposed models can provide more information than the ADC; and ii) to compare the models themselves in terms of fitting performance in order to see which hypothesis is more likely to explain the signal changes. Thus, (i) leads to new clinical indices of prion pathology and for a better characterization of specific features of the affected tissue, while (ii) aims for a general understanding of the pathological mechanism responsible for the signal hyperintensity.

2. Material and methods

2.1. Subjects

We recruited 15 consecutive patients with suspected diagnosis of prion disease and four healthy age-matched elderly subjects. The

study was approved by the local ethical committee and all individuals or their caregivers signed informed consent.

The diagnostic protocol included general clinical assessment, neurological evaluation, polygraphic EEG recording, analysis of the *PRNP* gene, cerebral MRI and blood laboratory tests, CSF analysis for the presence of 14-3-3 and the levels of total tau protein was performed in 11 patients. Diagnosis of "probable" sCJD was made according to the current diagnostic criteria (Zerr et al., 2009). Lack of brain tissue examination impeded PrP^{Sc} type determination. However, one of six molecular subtypes (MM1, MV1, MM2, MV2, VV1 and VV2) was tentatively assigned to sCJD patients by three neurologists with expertise in prion disease (V.R., P.G., F.T.) using available clinical data.

2.2. MR imaging acquisition

The study was performed on a 1.5 T MR imaging unit (Siemens Avanto, Erlangen, Germany). The imaging protocol consisted of 264 DWIs and 26 interleaved b = 0 volumes, using a twice-refocused (Reese et al., 2003) single shot spin-echo echo-planar imaging (SS-SE EPI) sequence with four independent diffusion gradient directions, a TR of 7.2 s, nine values of TE in the range of 68–107 ms and 13 b-values in the range of 250–9000 s mm^{-2}. For each TE, all the b-values were used up to the maximum available for that TE, according to the scheme in Inline Supplementary Table 1, and the four gradient directions were oriented in accordance to the tetrahedral symmetry, to take advantage of the maximum physical gradient strength. 45 slices were acquired, with a FOV of 220×220 mm^2 and an isotropic resolution of $2.3 \times 2.3 \times 2.3$ mm^3. At each value of TE, the increasing b-values were achieved by increasing the gradient strength with the timings of the gradient pulses fixed, and thus the intrinsic timescale of the measurement. However, as TE increased, the lengths of the gradient pulses increased, which provided measurements associated with longer diffusion times. The twice-refocused single-shot spin-echo (SS-SE) sequence has no single associated diffusion time, but measurements with longer TE are sensitive broadly to dispersion over longer diffusion times. The combination of measurements sensitive to different time scales and diffusion weightings enables estimation of pore sizes (Clayden et al., 2009). The range of pore diameters to which we have sensitivity, with the gradient strength available on the Avanto system, is approximately 5–20 μm (Clayden et al., 2009; Dyrby et al., 2013), which is typical of vacuole sizes in prionopathies (Kovacs and Budka, 2008).

Inline Supplementary Table S1 can be found online at http://dx.doi.org/10.1016/j.nicl.2014.11.017.

Additionally, a clinical diffusion weighted SS-SE EPI sequence (TR = 3800 ms, TE = 74 ms, b-values 500 and 1000 s mm^{-2}, 30 slices, FOV 230×230 mm^2, in-plane resolution 1.8×1.8 mm^2, slice thickness = 3.5 mm), a T_2-weighted FLAIR (TE/TR/TI 121/8000/2500 ms, flip angle 150°, 25 coronal slices, slice thickness 5 mm, in-plane resolution 0.78×0.78 mm^2) and a volumetric T_1-weighted magnetization-prepared rapid acquisition gradient-echo sequence (MPRAGE, TE/TR/TI 3.61/2400/1000 ms, flip angle 8°, 160 sagittal slices, slice thickness 1.2 mm, in-plane resolution 1.25×1.25 mm^2) were acquired. The total acquisition time was about 45 min.

2.3. Imaging analysis

Images were corrected for head motion using FLIRT (FMRIB's Linear Image Registration Tool, University of Oxford, U.K., Jenkinson et al., 2002). An affine transformation with 12 degrees of freedom was calculated to register each b0 volume to the first one and then applied to transform the subsequent DWIs into the same space.

Regions of interest (ROIs) were manually drawn by an expert neuroradiologist in the following areas in the cortex and basal nuclei of each subject: hippocampus (Hip), inferior temporal gyrus (ITG), superior temporal gyrus (STG), caudate nucleus (Cau), anterior putamen (aPut), dorso-medial thalamus (DMTh), occipital cortex (Occ), inferior parietal lobule (IPL), superior parietal lobule (SPL), precuneus (PreCu), anterior middle frontal gyrus (aMFG), superior frontal gyrus (SFG), and anterior cingulate cortex (ACC). Each area was delineated in both hemispheres and on multiple slices. In sCJD patients each ROI was classified as affected or unaffected according to the presence or absence of signal hyperintensity on DWI and if affected the delineation was limited to the area of evident hyperintensity. The MR signal of each ROI was averaged over all voxels and slices included by the ROI.

2.4. Models

The three models mentioned in the introduction were considered. We started from a general form of each model and then simplified them by adding some constraints on the parameters, as specified in Appendix A. The final forms are the following:

- The biexponential model is

$$S = M_0 \cdot e^{-\frac{TE}{T_2}}[f \cdot e^{-b \bullet d_1} + (1-f)e^{-b \cdot d_2}] \quad (1)$$

where the five free parameters are: M_0, which is a steady-state magnetization parameter reflecting proton density; the T_2 relaxation parameter; d_1 and d_2, the apparent diffusivities in the two compartments; and f, the volumetric fraction of the first compartment.

We associate this model with hypothesis (a) in the introduction: reduced diffusivity due to PrP^{Sc} deposition. If PrP^{Sc} deposition only is responsible for DWI hyperintensity, we expect to find a reduction of diffusivity in at least one of the two compartments as the most significant difference between patients and controls. If we can associate the two diffusivities with the intra and extracellular compartments, as Clark and Le Bihan (2000) suggest, then we expect to see the reduction in the extracellular compartment, which is normally that with the higher diffusivity.

- The restricted diffusion model has two compartments, one with restricted diffusion in a spherical pore (the vacuole), and the other with isotropically hindered diffusion. Mathematically, the model is:

$$S = M_0 \cdot e^{-\frac{TE}{T_2}}[f \cdot Sph(b, TE, d_R, R) + (1-f)e^{-b \cdot d_H}] \quad (2)$$

where $Sph(b,TE,d_R,R)$ is the expression for the signal from water restricted inside a sphere, which uses the Gaussian phase distribution approximation, as in Murday and Cotts (1968), but adapted for the twice-refocused spin echo sequence as described in Clayden et al. (2009). The *Sph* model has two free parameters: the radius R of the sphere and d_R, the intrinsic diffusivity inside the spherical compartment, which we fixed to the diffusivity of free water at body temperature (3×10^{-9} m^2/s), since vacuoles contain mostly water.

The other free parameters of this model are M_0 and T_2, as in the biexponential model, the apparent diffusivity in the hindered compartment, d_H, and the volumetric fraction of the restricted compartment, f, for a total of five free parameters.

We associate this model with hypothesis (b) in the introduction: restriction in the vacuoles (the spherical compartment). If DWI hyperintensity is caused by restriction in the vacuoles, we expect to observe an increase of f in the patients compared to the healthy subjects. Indeed the volume fraction of the restricted compartment (the percentage of the tissue occupied by restricting spheres) quantifies the extent of isotropic restriction, while the radius of the sphere reflects the size of the restricting structures. If hypothesis (b) is true, these two parameters should be markers of vacuolization and vacuolar size, respectively.

Table 1
Clinical data, MR imaging and laboratory test results for the 15 patients and 4 healthy controls.

Patient code	Sex	Age at onset (years)	Total disease duration (mos)	Disease duration at MRI (mos)	Clinical findings						PRNP mutation
					Initial signs	Full stage					
						Dementia	Cerebellar /visual	Pyramidal/ Extrapyr signs	Behavioural disorder	Mioclonus	
CJD01	F	60	14	2	cognitive deficits	1	1	0	1	1	E200K
CJD02	M	61	5	2	cognitive deficits	1	1	0	0	0	0
CJD03	M	75	7	6	ataxia	1	1	1	0	0	0
CJD04	M	74	8	7	parkinsonism	1	0	1	1	1	0
CJD05	F	55	29	3	cognitive deficits	1	0	0	1	0	0
CJD06	M	70	24	24	ataxia	1	1	1	0	1	0
CJD07	M	69	3	2	cognitive deficits	1	1	1	1	1	0
CJD08	F	65	38	23	cognitive deficits	1	0	1	1	0	0
CJD09	M	64	17	8	ataxia	1	1	0	0	0	0
CJD10	F	73	16	2	cognitive deficits	1	0	1	0	1	0
GSS01	M	32	45	12	ataxia	0	1	0	0	0	P102L
GSS02	F	56	33	3	ataxia	0	1	0	0	0	P102L
RPE01	M	59	NA	10	cognitive deficits	1	0	0	0	0	0
RPE02	F	80	8	5	ataxia	0	1	0	0	0	0
RPE03	M	81	NA	4	cognitive deficits	1	0	0	1	0	0
HC01	F	66	-	-	-	0	0	0	0	0	-
HC02	M	59	-	-	-	0	0	0	0	0	-
HC03	M	59	-	-	-	0	0	0	0	0	-
HC04	M	63	-	-	-	0	0	0	0	0	-

The sCJD molecular subtype (MM1, MM2, MV1, MV2, VV2) was assigned to each patient according to the clinical data indicated in this table.
Abbreviations: CJD = Creutzfeldt-Jakob disease; GSS = Gerstmann–Sträussler–Scheinker syndrome; RPE = rapidly progressive encephalopathy; HC = healthy control; F = female; M = male; 1 = positive; 0 = negative; PRNP = PRioN Protein; MM=Methionine-Methionine; MV=Methionine-Valine; VV=Valine-Valine; NA = not applicable; ND = not determined; sCJD = sporadic Creutzfeldt-Jakob disease.

Table 1 (*continued*)

Patient code	PRNP codon 129	14-3-3	Tau (pg/ml)	DWI	EEG	Predicted sCJD molecularsubtype	Average Radius in ROI with signal hyperintensity	Average Radius in ROI without signal abnormality	Clinical Diagnosis
CJD01	MV	ND	ND	1	0	-	5,54	0,2	familial CJD
CJD02	VV	positive	15432	1	0	VV2	6,07	2,58	sCJD
CJD03	MV	ambiguous	6983	1	1	MV2	4,13	1,84	sCJD
CJD04	MM	ND	ND	1	1	MM1	4,37	3,33	sCJD
CJD05	MM	positive	2100	1	1	MM2	5,16	6,54	sCJD
CJD06	VV	positive	2062	1	0	VV2	4,87	2,62	sCJD
CJD07	MV	positive	2113	1	1	MV1	4,45	1,29	sCJD
CJD08	MV	ambiguous	1648	1	0	MV2	7,32	8,02	sCJD
CJD09	MV	positive	617	1	0	MV2	5,37	6,71	sCJD
CJD10	MV	positive	2390	1	1	MV2	7,07	3,91	sCJD
GSS01	MM	negative	462	0	0	-	NA	1,85	GSS
GSS02	MM	ND	ND	0	0	-	NA	2,53	GSS
RPE01	-	negative	267	0	0	-	NA	3,04	autoimmune encefalopathy
RPE02	-	ambiguous	637	0	0	-	NA	0,86	paraneoplastic encefalopathy
RPE03	-	-	-	0	0	-	NA	2,53	paraneoplastic encefalopathy
HC01	-	-	-	0	-	-	NA	NA	Normal
HC02	-	-	-	0	-	-	NA	NA	Normal
HC03	-	-	-	0	-	-	NA	NA	Normal
HC04	-	-	-	0	-	-	NA	NA	Normal

• The mono-exponential model is:

$$S = M_0 e^{-\frac{TE}{T_2}} e^{-b \cdot ADC} \quad (3)$$

with three free parameters: M_0, T_2 and ADC.

This is a simple standard model, which we include primarily to compare our results with literature, and to understand what information the more complex models can add.

2.5. Model fitting

The three models described in Section 2.4 were fitted to the mean DWI signal in each ROI. We followed a fitting procedure similar to that in Panagiotaki et al. (2012); the details are reported in Appendix B.

2.6. Model comparison

The Bayesian Information Criterion (BIC, Schwarz, 1978) was used to compare the performance of the different models (see Appendix B; a worse fitting performance results in a higher BIC value). All the described procedures were implemented in MatLab (The Mathworks, Natick, MA, USA).

2.7. Statistical analysis

For each anatomical area, the 38 ROIs (two ROIs per subject, in the left and right hemispheres respectively) were divided in five groups: CJD+ (i.e. affected ROIs in CJD patients), CJD− (i.e. unaffected ROIs in CJD patients), HC (i.e. ROIs in healthy controls), RPE (i.e. ROIs in patients with Rapidly Progressive Encephalopathy) and GSS (i.e. ROIs in patients with Gerstmann–Sträussler–Scheinker syndrome); see Table 1 for the diagnostic classification of patients.

Since in the biexponential model the two terms in Eq. (2) have the same expression, they are randomly associated with the "fast" component (higher diffusivity) and the "slow" one (lower diffusivity) respectively. After the fitting procedure, we renamed the higher value between $d1$ and d_2 as d_F and the lower one as d_S in order to make them more comparable between subjects. Accordingly, we redefined f as the fraction of the fast component.

The mean raw signal for each combination of acquisition parameters was compared between CJD patients and controls, to understand which combination is most sensitive to the anomalies.

The mean value and standard deviation of each estimated parameter were calculated in each group, and a one-tailed t-test was used to test the statistical significance of differences between each of the pathological groups and the healthy controls, both considering all the ROIs in each group together and considering the different anatomical areas separately.

3. Results

3.1. Patients

Relevant clinical and laboratory data of the study population are reported in Table 1. Of the 15 patients enrolled in the study with suspected prion disease, nine were diagnosed as "probable" sCJD according to the current criteria (Zerr et al., 2009), one as familial CJD associated with the E200K *PRNP* mutation, two as GSS linked to the P102L *PRNP* mutation, and three as autoimmune encephalopathy. Cognitive deficits were the initial sign of disease in six patients with CJD and two with autoimmune encephalopathy, while ataxia was the presenting symptom in three patients with CJD, one with autoimmune encephalopathy and the two patients with GSS. One patient with CJD presented with parkinsonism. DWI signal hyperintensity in the cerebral cortex and/or striatum was observed in all CJD patients, while no signal abnormalities were detected in the individuals with GSS or autoimmune encephalopathy.

3.2. Raw MR signal intensity

A typical case of sCJD with signal hyperintensity in the cortical ribbon on DWI and FLAIR is illustrated on Fig. 1. The signal abnormality is much more prominent on DWI with b = 1000 than with b = 500, FLAIR and T2WI in this decreasing order. ADC maps show decreased diffusivity in the affected regions.

The mean raw signal in the CJD+ regions was higher than in CJD− regions and in HC with all the considered combinations of b-value and TE (Fig. 2A); this increase was consistent across all the parameter combinations and significant in almost all of them. The signal in CJD− regions was slightly higher than in controls, but the difference was never significant.

Since the human eye is sensitive to contrast rather than to absolute signal, we calculated the relative difference of the raw signal between each pair of groups (Fig. 2B). The contrast increased with b-value and TE reaching a peak with b = 3000 s/mm^2 and TE = 103 ms, then slightly decreasing for even higher b-values. The estimated contrast-to-noise ratio (CNR) at the peak was about 5.5, which was sufficiently high to prove that the hyperintensity was not masked by noise.

3.3. Model fitting performance

The quality of fit was good for the biexponential and restricted-diffusion models and the two models predict very similar signals, while the mono-exponential model predicts quite different signals at high b-values (see Fig. 3).

The BIC score was considered as a quantitative index of the fitting performance of the three models in each group of ROIs (Table 2). In the affected ROIs (CJD+) the biexponential and restricted-diffusion models performed significantly better than the mono-exponential model although they performed very similarly to one another (the difference was not significant). Thus, although the fitting results did not show that either of the two hypotheses about the origin of the signal hyperintensity was better than the other, they did show that both the bi-compartment models provided a better fit to the data than the standard mono-exponential model and so should provide more sensitive and specific parameters. Also in the CJD− group and in controls we found no significant difference between the two bi-compartment models and a significant decrease of BIC in both of them compared to the mono-exponential model, but this decrease was lower than in CJD+.

We also observed that the BIC was always significantly higher in the affected regions than in the healthy ones; this suggests that neither of our models fully explains the MRI signal in affected areas, but the increased difference between the mono-exponential and the bi-compartment models described above means that the proposed models allow a considerably better characterization of the pathological signal than the traditional one.

3.4. Differences in estimated MR parameters among groups

The results of the comparison among each patient group and healthy controls are reported in Table 3; results for each anatomic region are reported in Inline Supplementary Tables 2–6.

Inline Supplementary Table S2 can be found online at http://dx.doi.org/10.1016/j.nicl.2014.11.017.

Inline Supplementary Table S3 can be found online at http://dx.doi.org/10.1016/j.nicl.2014.11.017.

Inline Supplementary Table S4 can be found online at http://dx.doi.org/10.1016/j.nicl.2014.11.017.

Inline Supplementary Table S5 can be found online at http://dx.doi.org/10.1016/j.nicl.2014.11.017.

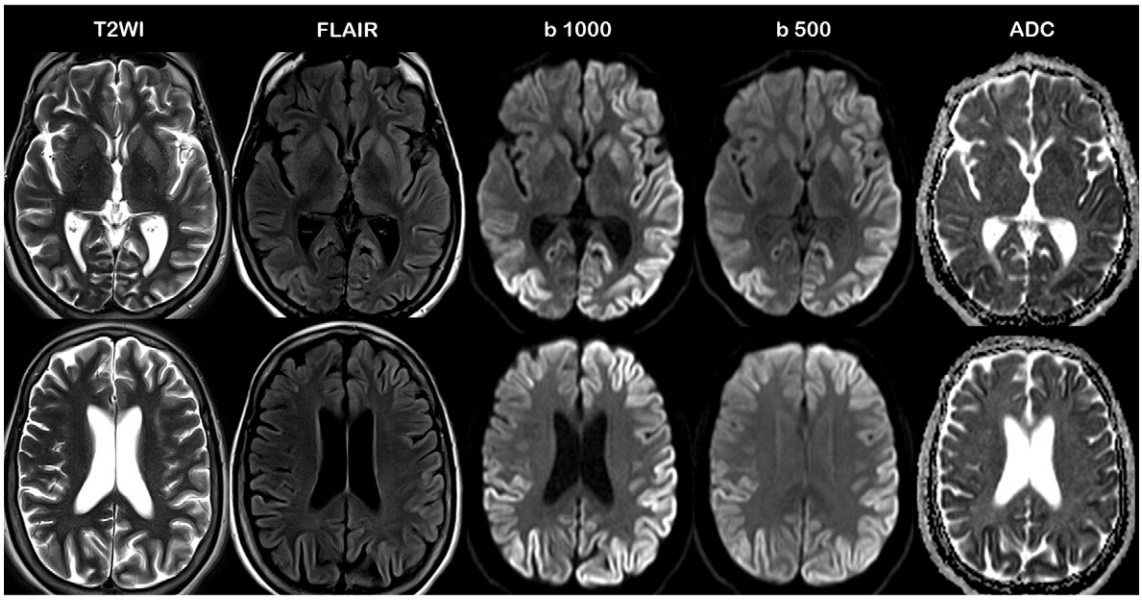

Fig. 1. MR images used for clinical diagnosis of sCJD in one patient with sCJD acquired at the level of the basal nuclei and lateral ventricles. Affected (CJD+) regions look bright and are more prominent on DWI with b = 1000 than b = 500, FLAIR and T2WI respectively in this order. Affected regions with decreased diffusivity look darker on ADC maps. Note the asymmetry of signal hyperintensities that in this patient are more extensive in the left cerebral hemisphere than in the right, basal nuclei and thalami.

Inline Supplementary Table S6 can be found online at http://dx.doi.org/10.1016/j.nicl.2014.11.017.

3.4.1. CJD + vs. healthy controls

In the affected regions of CJD patients (CJD+ group) we found an increase of T_2, a decrease of diffusivities and an increase of the fraction of the restricted compartment with respect to controls (Table 3).

T_2 was significantly increased in CJD+ in almost all the areas and in all three models (Fig. 4B). Lengthening in T_2 relaxation time was greatest in the frontal cortex, while it was lower in the parietal and temporal areas. Minor differences were observed when comparing the different models.

The proton density, M_0, was significantly increased in the temporal cortex and decreased in most of the other areas; some inconsistencies were observed among the three models, thus this parameter was not very informative.

Diffusivities were generally reduced in all three models. In the biexponential model, d_F was significantly reduced in PreCu, SFG, aMFG, SPL and aPut (Fig. 4C), while d_S was reduced in PreCu, SFG, aMFG, STG, SPL IPL and Occ (Fig. 4D); in most of the other areas d_F

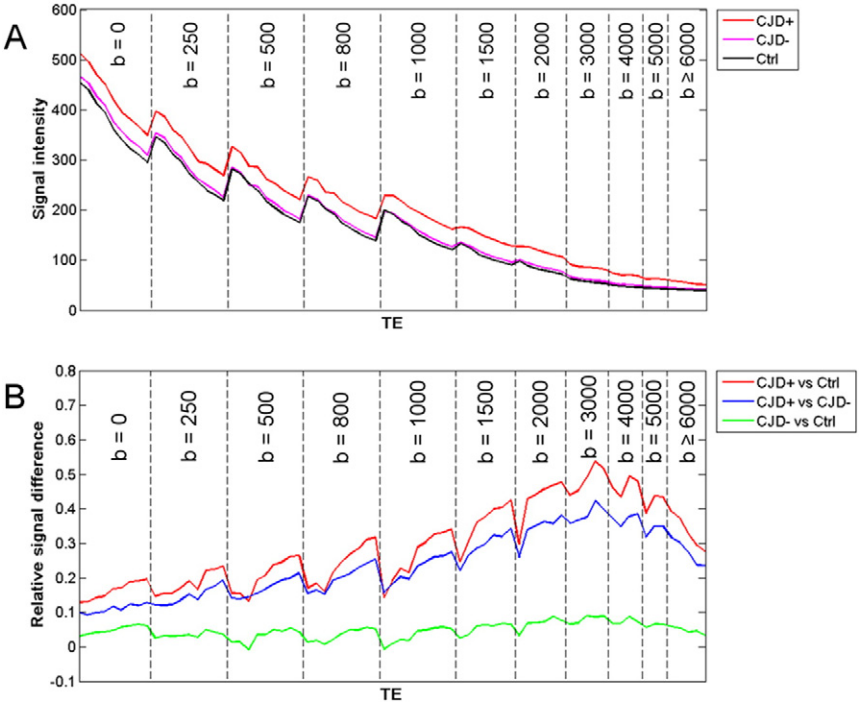

Fig. 2. Raw signal in the different groups. A) Raw signal in the three main groups at each combination of the acquisition parameters. B) Relative difference between the mean signal in each pair of groups at each combination of the acquisition parameters.In both the plots, for any b-value reported on the graph, the TE grows from left to right (see the TE values applied at each b-value in Inline Supplementary Table 1).

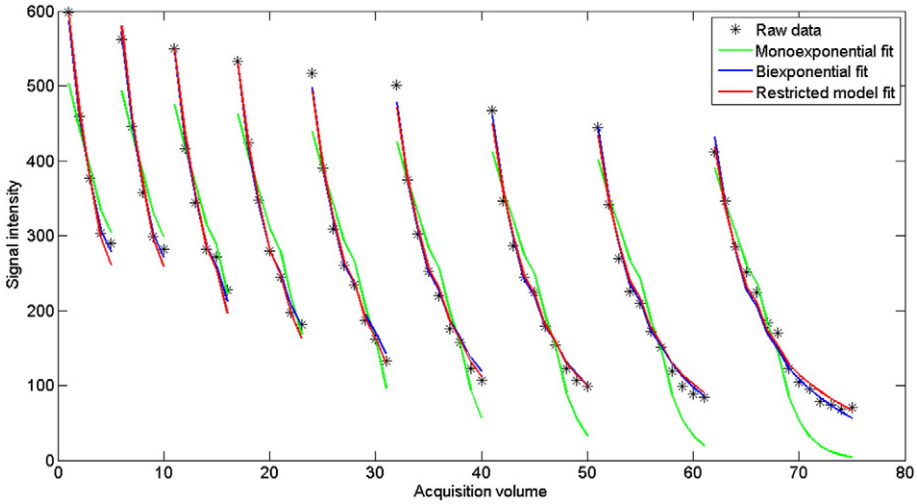

Fig. 3. Visual assessment of the quality of fit in a representative ROI of a CJD patient. The raw signal (stars) and the signal predicted by each model (solid lines with different colours) are shown for every volume acquired. See Supplementary Table 1 for the acquisition parameters applied.

and d_S decreased, even though not significantly. In the restricted-diffusion model, the differences in d_H were not significant in most anatomic regions. In the mono-exponential model, the *ADC* was significantly reduced in all the anatomical areas (Fig. 4E).

Differences in the fraction of the "fast" component of the biexponential model varied with the anatomical position: the fraction was significantly increased in the frontal and parietal lobes and in PreCu, significantly decreased in Cau and DMTh.

The fraction of the spherical compartment in the restricted-diffusion model was significantly increased in all the areas but Hip (Fig. 4F). The increase was particularly important (greater than 40%) in the temporal and parietal cortex, PreCu and DMTh.

In all regions of the CJD+ group the mean radius of the spherical compartment was in the range between 3 and 10 μm, compatible with the dimensions of the vacuoles in CJD as measured by histopathology (Kovacs and Budka, 2008), while in the control group the radii were generally much smaller (about 1.6 μm on average). When averaged across all the affected ROIs, the mean radius was larger (about 7 μm) in 2 patients (CJD08 and CJD10) compared to the other 8 patients (3–6 μm) (Fig. 5A). Differences in size were observed also among anatomical areas: the radius was greater in SPL, PreCu, DMTh and Occ, while it was smaller in frontal regions (aMFG, SFG, and ACC) (Fig. 5B).

The percentage of difference of each estimated parameter in each region is specified in Inline Supplementary Table 3.

3.4.2. CJD− vs. healthy controls

The relative alterations of T_2 and of the fraction of the restricted compartment between the CJD− group and the control group (Table 3 and Inline Supplementary Table 4) were generally smaller and less statistically significant, but followed the trend of those reported above for the CJD+ group. The radius of the spherical compartment in CJD− was significantly larger than in healthy and pathological controls ($p < 0.001$) but smaller than in CJD+ regions ($p < 0.001$).

On the contrary in the CJD− group there was no significant change in diffusivity in the mono-exponential model (i.e. *ADC*), in the biexponential model (i.e. d_F and d_S) nor in the restricted-diffusion model (i.e. d_H). This result suggests that the models tend to explain the appearance of signal hyperintensity on DWI as a reduction of diffusivity (biexponential model) or increase of intra-vacuolar volume fraction (restricted model).

3.4.3. RPE and GSS patients vs. healthy controls

In the RPE group we observed a slight increase of T_2 and diffusivities in comparison with healthy controls (Table 3 and Inline Supplementary Table 5), while in the GSS group we found just few sporadic anatomic reductions of M_0 and T_2 (Inline Supplementary Table 6).

3.4.4. CJD+ vs. RPE, GSS and controls

We also compared the CJD+ group with the RPE and GSS groups and with a "generalized" control group including all the ROIs in non-CJD subjects (controls, RPE and GSS). In all three comparisons we found similar results as between CJD+ and healthy controls. These results demonstrated that increased T_2, decreased diffusivities and increased intracellular volume fraction are the main changes in MR parameters associated with regions of DWI signal hyperintensity.

Table 2
Mean BIC values for each model in CJD+, CJD− and HC ROIs.

BIC values	CJD+	CJD−	HC
Biexponential	2277 ± 141 (*,#)	2106 ± 156 (*)	2022 ± 80 (*)
Restricted	2287 ± 141 (*,#)	2116 ± 156 (*)	2031 ± 86 (*)
Mono-exponential	2633 ± 367 (#)	2305 ± 291 (#)	2143 ± 163

Higher values are associated with worse fitting performances. Values marked with (*) are significantly lower than the mean BIC of the mono-exponential in the same group of ROIs, showing a better fitting performance of the bi-compartment models with respect to the traditional one. Values marked with (#) are significantly higher than the mean BIC of the mono-exponential in the HC group, showing a worse fitting performance with respect to the normal case, probably due to pathological changes not fully explained by the models.

Table 3
Results of the group analysis. Mean relative difference in each parameter between each group (CJD+, CJD−, RPE or GSS respectively) and the healthy controls.

		CJD+	CJD-	RPE	GSS
Biexponential	M_0	n.s.	n.s.	n.s.	n.s.
	T_2	+26%	+10%	n.s.	n.s.
	d_F	-14%	n.s.	n.s.	n.s.
	d_S	-37%	n.s.	-20%	n.s.
	f	+4%	n.s.	+9%	n.s.
Restricted	M_0	n.s.	n.s.	n.s.	n.s.
	T_2	+18%	+8%	n.s.	n.s.
	d_H	n.s.	+8%	+10%	n.s.
	f	+46%	+19%	n.s.	n.s.
Monoexp	M_0	-8%	n.s.	n.s.	n.s.
	T_2	+31%	+12%	+5%	n.s.
	ADC	-20%	n.s.	+5%	n.s.

Abbreviations: n.s. = not significant.

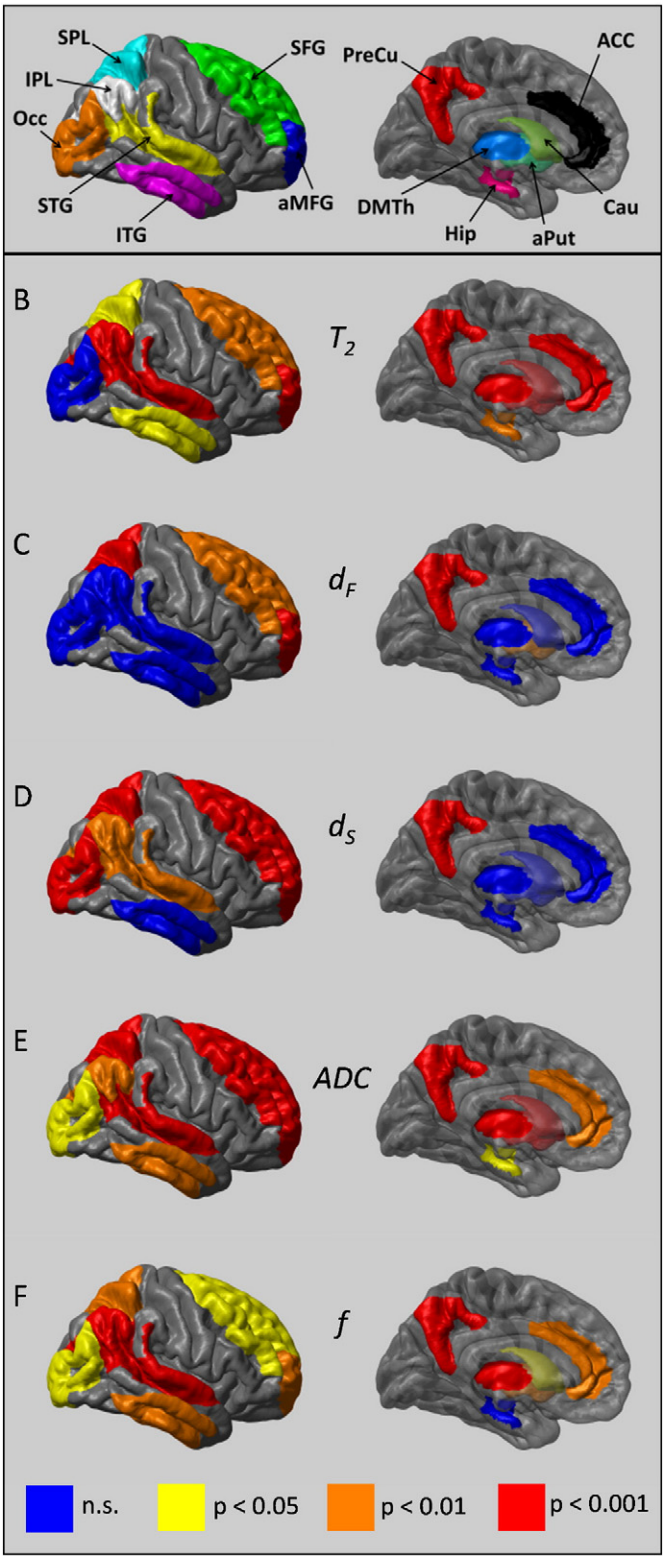

Fig. 4. Tridimensional representation of the regional dependence of statistical differences in the estimated parameters. A) 3D rendering of the cortical and subcortical areas considered in the ROI-based analysis. B–F) Representation of the statistical significance of the differences between CJD+ and HC for the main parameters: T_2 in the mono-exponential models (B) and d_F (C) and d_S (D) in the biexponential model; *ADC* in the mono-exponential model (E); the volumetric fraction of the spherical restricted compartment in the restricted-diffusion model (F). In each panel the analysed areas without significant differences are in blue, while the areas with statistically significant differences are in yellow ($p < 0.05$), orange ($p < 0.01$) or red ($p < 0.001$).

4. Discussion

In this prospective study we have used mathematical models to analyse differences in MR DWI signal acquired in patients with suspected prion disease and controls. Data were acquired with an advanced imaging protocol using many combinations of TE, diffusion weightings and times that allowed an in-depth analysis of the MR signal abnormality. For the first time we provided an estimate of the radius of the restricted compartment that in affected ROIs may be related to the presence and size of vacuoles. The estimated vacuole size in affected regions was in the range between 3 and 10 μm that is compatible with the dimensions of the vacuoles as measured by neuropathology in sCJD. In healthy subjects and in non-CJD patient groups the restricted fraction was quite small, that may suggest that there is no source of proper restriction. The results of the model-based analysis showed significantly longer T_2, lower diffusivity, or greater fraction of restricted diffusion in DWI hyperintense areas.

A first analysis performed on raw MR signal showed a significantly higher signal in the CJD+ group with respect to healthy subjects, GSS and RPE, across the whole range of b-values. The absolute difference between the signal in CJD+ and controls in each ROI appears almost constant across different echo times and b-values. The relative difference in MR signal tends to increase with both b and TE, reaching a maximum at $b = 3000$ s/mm^2 and $TE = 103$ ms, which indicates an optimal operating point. Since the relative signal difference is closer to the contrast seen by human eye than the absolute signal. Our results are in agreement with previous studies (Hyare et al., 2010a; Riva-Amarante et al., 2011) which suggested the use of high b-values ($b = 3000$) for better contrast of CJD lesions.

In the second part of the study we analysed the MR signal intensity with three mathematical models: biexponential, spherical restricted-diffusion and mono-exponential. This is the first study probing CJD with diffusion models more complex than the mono-exponential one, derived from two hypotheses about the origin of the hyperintensity on DWI and FLAIR MR images in CJD patients. The aims of the model-based analysis were (i) to evaluate the differences in the parameters of each model associated with CJD, and (ii) to compare the models themselves to understand the underlying neuropathological substrate. As for aim (i), the statistical analysis highlighted some consistent differences: in CJD patients the T_2 value is markedly increased in almost all hyperintense affected regions, the diffusivities are generally reduced in the mono- and biexponential models, and the fraction of the spherical compartment estimated by the restricted-diffusion model is increased. Although the *ADC* is the only parameter to show statistically significant differences in all the areas, this does not support the mono-exponential model. The biexponential and restricted-diffusion models also show statistically significant differences in all the areas, but the particular MR parameter explaining the difference changes: the models pin down the source of the statistical differences more precisely to particular parameters that are not the same in different anatomic regions.

The *ADC* numerical values found for CJD patients and controls in our study are compatible with those reported by previous works that have shown a reduction in ADC in CJD patients (Demaerel et al., 2003; Tschampa et al., 2003; Hyare et al., 2010b). For the other MR parameters there are no previous numerical results in the literature, but our quantitative results are in agreement with qualitative results reported in many clinical studies about the sensitivity of different MRI sequences to the detection of CJD. In particular, according to our results both the T_2-weighted and the diffusion-weighted component of the signal are altered; so FLAIR and T_2-weighted sequences can detect the pathology to some extent due to the alteration of T_2, but DWI sequences are much more sensitive because they include both weightings (i.e. T_2 and diffusion). The increase of the T_2 relaxation time may be related to neuronal loss, resulting in a more homogeneous microenvironment due to reduction of microstructural components that cause surface relaxation.

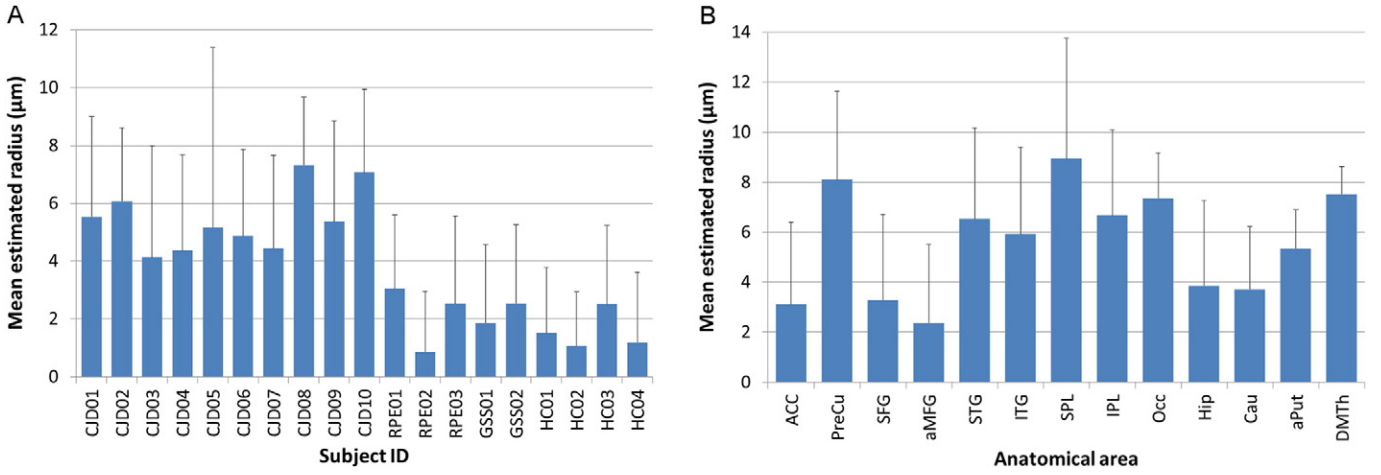

Fig. 5. Estimated radius of the spherical compartment in the different subjects and areas. A) Histogram showing the estimated radius averaged across all the ROIs in each subject. B) Histogram showing the estimated radius averaged across all the CJD+ ROIs in each anatomical area.

This is the first study attempting to measure vacuolar average size. A significant increase in the radius of the spherical compartment was found in sCJD patients compared with all controls, even though a direct comparison is not very meaningful because the restricted fraction is quite small in the controls where vacuoles are absent. A very small restricted fraction may suggest that there is no source of restriction at all; the relatively small mean diameter of the restricted compartment suggests that the cause of restriction, if present, may be due to subcellular structures. The estimated radius of the spherical restricted compartment in affected regions was in the range between 3 and 10 μm on average, compatible with the dimension of the vacuoles in CJD as measured by histopathology (Kovacs and Budka, 2008). This supports the association of the restricted portion of signal with the vacuoles, and that the radius of the sphere is an estimation of the average size of the vacuoles in the considered ROI or voxel. If confirmed on a larger group of patients with pathology-proven sCJD subtype, these results might have implications for early in vivo diagnosis of sCJD subtype. We also found interesting differences in average vacuolar size among anatomical areas; for example the estimated radius was smaller in the frontal lobes, cingulate, hippocampus and caudate, and larger in the thalamus, parietal and occipital lobes. This variation may reflect genuine differences in vacuole size, although other factors, such as differences in vacuole membrane permeability, may also influence the estimate.

Interestingly, in the "unaffected regions" of CJD patients (CJD− group) we found an increase of T_2 and of the fraction of the spherical compartment in the restricted-diffusion model (although lower than in affected CJD+ regions), but no coherent changes in diffusivities. These results suggest that perhaps the pathological alterations in regions without MR signal hyperintensity might be at subclinical stage.

Only minor differences in MR parameters were found in GSS and RPE patients with respect to healthy subjects; furthermore, we found almost the same differences between the CJD+ group and each of the three control groups (healthy, GSS and RPE). GSS is a genetic form of prion disease characterized by accumulation of N- and C-terminal truncated fragments of PrP in the form of amyloid plaques. Spongiform changes are usually absent or mild, except for a subgroup of patients with the P102L mutation showing a CJD-like phenotype. In patients with RPE the absence of MR signal abnormalities was an early clue to eventually rule out the diagnosis of sCJD. Thus we can conclude that the above reported differences in T_2, diffusivity and vacuolar volume fraction are specific to CJD and unlikely related to unspecific neuronal degeneration.

With regards to the specific pathological mechanisms altering diffusion properties, addressed in aim (ii), we observed that both the bi-compartment models have a better fitting performance than the mono-exponential one, and the difference in BIC is much greater in the affected ROIs than in the healthy tissue, even though the BIC values themselves are higher. Small differences in BIC values for healthy subjects show only small benefits of the more complex models compared to the mono-exponential, while in CJD+ the advantages of the more complex models are much more significant. Although our models cannot capture all the signal abnormality (because the BIC is always higher in CJD+ than in control ROIs) they represent a step towards a better characterization of the affected tissue, and some interesting observations can be inferred by a detailed analysis of the results.

Since the biexponential and the restricted-diffusion models have similar fitting performances, a possible explanation is that both pathological features of CJD may determine the MR signal abnormality to a similar extent. In affected ROIs water diffusion might be both hindered with lower diffusivity likely caused by prion PrP^{Sc} deposition in the extracellular space (hypothesis a) and restricted in vacuoles with impermeable barriers (hypothesis b). In the biexponential model the reduction of diffusivity occurs in both extra and intracellular compartments, which does not support hypothesis (a) directly, as this hypothesis implies a reduction only in the extra-cellular "fast" diffusion compartment. This observation does not refute hypothesis (a) because the assignment of components in the biexponential model to the intra and extracellular spaces is not strict (Clark and Le Bihan, 2000). However, in the restricted-diffusion model the differences between CJD+ and controls are found primarily in the restricted compartment and the diffusivity in the hindered compartment is almost never significantly altered. This finding somewhat goes against the combined hypothesis. Perhaps the biological mechanism involved in CJD is even more complex than we initially anticipated with the two hypotheses. Permeability of the vacuole walls is one possible mechanism that our models did not consider. It would reduce observable restricted diffusion and produce signal profiles closer to the biexponential model, as we observe. In addition, the actual size distribution of the hundreds of thousands of vacuoles present inside a relatively large voxel is likely less uniform than predicted by the mathematical model. Thus, a key area for further work is to study more sophisticated models, probably requiring more exotic measurements (Drobnjak et al., 2010; Lasic et al., 2011) that include these effects. A better understanding of the hallmark MR features will have an impact in designing new MR sequences and may improve detection of disease in prionopathies, especially in pre-symptomatic patients.

Another interesting question is the possibility to track progression of disease with the quantitative MR parameters considered in this study. It has been recently outlined that ADC changes follow a

more complex – neither linear, nor unidirectional – change with time (Caverzasi et al., 2014) with respect to other neurodegenerative diseases that follow a roughly linear or unidirectional decline. The development of severe brain atrophy on MRI is associated with the disappearance of the hyperintensity on DWI and ADC "pseudo-normalization" in about 1–4% of CJD Caucasian patients with a two-stage clinical course (so-called panencephalopathic form). The initial rapid deterioration is followed by an unusually prolonged state of akinetic mutism. We have examined one such patient with this same experimental diffusion protocol: in the severely atrophic cortical regions that were previously hyperintense on DWI, T_2 values and diffusivities were increased while the restricted fraction was decreased. These unique MRI results are in agreement with the neuropathological findings at autopsy reporting complete cortical cytoarchitecture collapse (status spongiosus), presence of large gliotic scars and neuronal loss with disappearance of the small vacuoles (Ghorayeb et al., 1998; Jansen et al., 2009). The "pseudo-normalization" of ADC in patients with unusually prolonged state of akinetic mutism is not related with the results of this study in the regions with DWI hyperintensity, since we considered separately cortical regions with and without DWI signal hyperintensity.

A few limitations of this study should be acknowledged. First of all, we have a clinical diagnosis for all the patients but not autopsy-proven results: so we could not look for a correlation of MR parameters with neuropathological results. Regarding the acquisition protocol, the twice-refocused SS-SE EPI DWI sequence available on our scanner has advantages from the point of view of image quality, but does not allow setting the diffusion time independently from the TE: a standard Stejskal–Tanner sequence could help obtaining clearer results on the dependence of the signal on the acquisition parameters. Moreover, even though the ROIs were carefully drawn not to exceed GM the 2.3 mm isotropic spatial resolution used was in the range of cortical thickness, therefore we cannot exclude some partial volume effects with WM. Finally, more sophisticated models could be investigated, as discussed above.

In conclusion, we thoroughly examined DWI data acquired with a wide range of T_2 and diffusion weightings and diffusion times in CJD patients. By comparing the raw MRI data of patients and healthy subjects we investigated the dependence of the observed signal hyperintensity on the acquisition parameters and we were able to suggest optimal MRI parameters that may further highlight such hyperintensities in future clinical studies. We showed that a biexponential or a spherical restricted-diffusion model can fit the data better than the generally used mono-exponential model. In the affected ROIs we found that the main contributions to DWI signal hyperintensity come from an increase of T_2 and some form of reduction of the diffusive motions, which is explained as a reduction of diffusivities by the mono- and biexponential models and as an increase of the restricted compartment in the spherical restricted-diffusion model. Since the two bi-compartment models performed similarly, we cannot conclude that either prion PrP^{Sc} deposition or spongiform degeneration is a more likely cause of DWI hyperintensities. Both pathological changes may contribute to the signal abnormality or the degree of complexity of microstructural pathology is higher than anticipated by the two models investigated in this study. Future studies will have to test more sophisticated models, for example accounting for vacuole permeability. For the first time we were able to show that it is feasible to estimate average vacuolar size with MRI. We believe that this work represents an important step forward to a better characterization of MRI abnormalities in prionopathies and to foster the development of more sensitive sequences for early diagnosis of sCJD.

Acknowledgements

This work was supported by a grant of the Consortium of Neuroimagers for the Noninvasive Assessment of Brain Connectivity and Tracts (CONNECT), funded by the European Commission under Framework Package 7. Additionally, MF's work was supported by MIUR, FIRB project "Materiali fluorurati nanostrutturati come mezzi di contrasto intelligenti in 19F-RMN (FLUORIMAGING)" project no. RBAP1183B5, DCA's work was supported by EPSRC with grants EP/G007748 and EP/I027084/01, PG's work was supported by CDC with grant UR8/CCU515004 and FT and VR's work was supported by the Italian Ministry of Health. The authors would like to thank Matteo Caffini, PhD for technical help in generating Fig. 4, and Raffaella Morini, PhD for assistance in drawing the graphical abstract.

Appendix A. Parameter constraints

As mentioned in the main text, we started from a more general form of the bi-compartment models, that is:

$$S = M_0[f \cdot e^{-\frac{TE}{T_{2,1}}} \cdot e^{-b \cdot d_1} + (1-f)e^{-\frac{TE}{T_{2,2}}} \cdot e^{-b \cdot d_2}] \quad \text{(A1)}$$

for the biexponential model and:

$$S = M_0\left[f \cdot e^{-\frac{TE}{T_{2R}}} \cdot Sph(b, TE, d_R, R) + (1-f)e^{-\frac{TE}{T_{2H}}} \cdot e^{-b \cdot d_H}\right] \quad \text{(A2)}$$

for the restricted-diffusion model.

The key difference between these equations and Eqs. (1) and (2) respectively is that a different T_2 is estimated in either compartment. We performed some preliminary fitting tests with these models and we noticed a certain degree of instability in the results. Furthermore, the $b = 0$ signal at various echo times showed no evidence of a biexponential trend, so we decided to fix the two T_2 parameters to be equal in both models.

An additional difference between the restricted-diffusion model in Eq. (A2) and its final form is that d_R (the intrinsic diffusivity in the restricted compartment) is a free parameter. However, from our preliminary tests we found that the results were insensitive to d_R, so we decided to fix d_R to a predetermined value; we chose the diffusivity of free water at body temperature (3×10^{-9} m^2/s) since vacuoles contain mostly water.

Thus the models took the simplified form shown in Eqs. (1) and (2) in the main text.

We also constrained the set of model parameters in the optimization using transformations that limit the range of each parameter to biophysically meaningful values. For all the models we constrained the T_2 values and the diffusivities to be positive and the volume fractions to be in [0, 1] and to sum to 1.

The reduction of the number of free parameters and the constraints on the allowed values were aimed at and stabilizing the fitting and parameter estimation.

Appendix B. Model fitting

We fitted each model to the data using an iterative non-linear optimization procedure from multiple starting points to avoid local minima. Here we used a Levenberg–Marquardt algorithm (Marquardt, 1963) for minimizing a chi-squared objective function with the Rician noise model (Sijbers et al., 1999; Alexander, 2008). The objective function is the negative log-likelihood:

$$F = -log(L) = \sum_{n=1}^{M}[2log\sigma - logI_0(\frac{S_n\tilde{S}_n}{\sigma^2}) + \frac{{S_n}^2 + {\tilde{S}_n}^2}{2} - logS_n] \quad \text{(B1)}$$

where L is the likelihood of the measurements given the model estimates, M is the number of measurements, σ is the standard deviation of the noise, $\tilde{S}_n$ is the nth measurement, S_n is the model predicted signal and I_0 is the zero-order modified Bessel function of the first kind. For all models, we chose the best fit parameters from the models after 100 perturbations of the starting parameters to ensure a good minimum.

Measurements below a noise-floor threshold, chosen from the estimated noise viance, were ignored during the fitting procedure.

The BIC (Schwarz, 1978) was calculated according to the following formula:

$$BIC = -2log(L) + k \cdot log(M) = 2F + k \cdot log(M) \quad \text{(B2)}$$

where L, M and F have the same meaning as in Eq. (B1), while k is the number of model parameters. It rewards the models that minimize the objective function, but it simultaneously penalizes those with a high number of parameters.

References

Alexander, D.C., 2008. A general framework for experiment design in diffusion MRI and its application in measuring direct tissue-microstructure features. Magn. Reson. Med. 60 (2), 439–448. http://dx.doi.org/10.1002/mrm.2164618666109.

Assaf, Y., Freidlin, R.Z., Rohde, G.K., Basser, P.J., 2004. New modeling and experimental framework to characterize hindered and restricted water diffusion in brain white matter. Magn. Reson. Med. 52 (5), 965–978. http://dx.doi.org/10.1002/mrm.2027415508168.

Barazany, D., Basser, P.J., Assaf, Y., 2009. In vivo measurement of axon diameter distribution in the corpus callosum of rat brain. Brain 132 (5), 1210–1220. http://dx.doi.org/10.1093/brain/awp04219403788.

Bizzi, A., Grisoli, M., Blevins, J., Giaccone, G., Port, J.D., Phillips, M.D., et al., 2009. MRI diagnostic accuracy in Creutzfeldt–Jakob disease: results of a multicenter study. Prion 2009: Book of Abstracts. Neuroprion, Chalkadiki, p. 85.

Caverzasi, E., Henry, R.G., Vitali, P., Lobach, I.V., Kornak, J., Bastianello, S., et al., 2014. Application of quantitative DTI metrics in sporadic CJD. Neuroimage Clin. 4, 426–435. http://dx.doi.org/10.1016/j.nicl.2014.01.01124624328.

Clark, C.A., Le Bihan, D., 2000. Water diffusion compartmentation and anisotropy at high b values in the human brain. Magn. Reson. Med. 44 (6), 852–859. http://dx.doi.org/10.1002/1522-2594(200012)44:6<852::AID-MRM5>3.0.CO;2-A11108621.

Clayden, J.D., Nagy, Z., Hall, M.G., Clark, C.A., Alexander, D.C., 2009. Active imaging with dual spin-echo diffusion MRI. Inf Process Med Imaging 21, 264–275. http://dx.doi.org/10.1007/978-3-642-02498-6_2219694269.

Demaerel, P., Sciot, R., Robberecht, W., Dom, R., Vandermeulen, D., Maes, F., et al., 2003. Accuracy of diffusion-weighted MR imaging in the diagnosis of sporadic Creutzfeldt–Jakob disease. J. Neurol. 250 (2), 222–225. http://dx.doi.org/10.1007/s00415-003-0983-612574955.

Drobnjak, I., Siow, B., Alexander, D.C., 2010. Optimizing gradient waveforms for microstructure sensitivity in diffusion-weighted MR. J. Magn. Reson. 206 (1), 41–51. http://dx.doi.org/10.1016/j.jmr.2010.05.01720580294.

Dyrby, T.B., Søgaard, L.V., Hall, M.G., Ptito, M., Alexander, D.C., 2013. Contrast and stability of the axon diameter index from microstructure imaging with diffusion MRI. Magn. Reson. Med. 70 (3), 711–721. http://dx.doi.org/10.1002/mrm.2450123023798.

Galanaud, D., Dormont, D., Haïk, S., Chiras, J., Brandel, J.P., Ranjeva, J.P., 2008. Differences of apparent diffusion coefficient values in patients with Creutzfeldt–Jakob disease according to the codon 129 genotype. A.J.N.R. Am. J. Neuroradiol. 29 (7), e57. http://dx.doi.org/10.3174/ajnr.A107518372408.

Galanaud, D., Haïk, S., Linguraru, M.G., Ranjeva, J.P., Faucheux, B., Kaphan, E., et al., 2010. Combined diffusion imaging and MR spectroscopy in the diagnosis of human prion diseases. A.J.N.R. Am. J. Neuroradiol. 31 (7), 1311–1318. http://dx.doi.org/10.3174/ajnr.A206920430851.

Gambetti, P., Kong, Q., Zou, W., Parchi, P., Chen, S.G., 2003. Sporadic and familial CJD: classification and characterisation. Br. Med. Bull. 66, 213–23914522861.

Gambetti, P., Cali, I., Notari, S., Kong, Q., Zou, W.Q., Surewicz, W.K., 2011. Molecular biology and pathology of prion strains in sporadic human prion diseases. Acta Neuropathol. 121 (1), 79–90. http://dx.doi.org/10.1007/s00401-010-0761-321058033.

Geschwind, M.D., Potter, C.A., Sattavat, M., Garcia, P.A., Rosen, H.J., Miller, B.L., et al., 2009. Correlating DWI MRI with pathologic and other features of Jakob–Creutzfeldt disease. Alzheimer Dis. Assoc. Disord. 23 (1), 82–87. http://dx.doi.org/10.1097/WAD.0b013e31818323ef19266702.

Ghorayeb, I., Series, C., Parchi, P., Sawan, B., Guez, S., Laplanche, J.L., et al., 1998. Creutzfeldt–Jakob disease with long duration and panencephalopathic lesions: molecular analysis of one case. Neurol. 51 (1), 271–274. http://dx.doi.org/10.1212/WNL.51.1.2719674819.

Hyare, H., Thornton, J., Stevens, J., Mead, S., Rudge, P., Collinge, J., et al., 2010a. High-b-value diffusion MR imaging and basal nuclei apparent diffusion coefficient measurements in variant and sporadic Creutzfeldt–Jakob disease. A.J.N.R. Am. J. Neuroradiol. 31 (3), 521–526. http://dx.doi.org/10.3174/ajnr.A186020007724.

Hyare, H., Wroe, S., Siddique, D., Webb, T., Fox, N.C., Stevens, J., et al., 2010b. Brain-water diffusion coefficients reflect the severity of inherited prion disease. Neurology 74 (8), 658–665. http://dx.doi.org/10.1212/WNL.0b013e3181d0cc4720177119.

Jansen, C., Head, M.W., Rozemuller, A.J., Ironside, J.W., 2009. Panencephalopathic Creutzfeldt–Jakob disease in the Netherlands and the UK: clinical and pathological characteristics of nine patients. Neuropathol. Appl. Neurobiol. 35 (3), 272–282. http://dx.doi.org/10.1111/j.1365-2990.2008.01004a.x19473294.

Jenkinson, M., Bannister, P., Brady, M., Smith, S., 2002. Improved optimization for the robust and accurate linear registration and motion correction of brain images. Neuroimage 17 (2), 825–841. http://dx.doi.org/10.1006/nimg.2002.113212377157.

Kallenberg, K., Schulz-Schaeffer, W.J., Jastrow, U., Poser, S., Meissner, B., Tschampa, H.J., et al., 2006. Creutzfeldt–Jakob disease: comparative analysis of MR imaging sequences. A.J.N.R. Am. J. Neuroradiol. 27 (7), 1459–146216908558.

Kiselev, V.G., Il'yasov, K.A., 2007. Is the "biexponential diffusion" biexponential? Magn. Reson. Med. 57 (3), 464–469. http://dx.doi.org/10.1002/mrm.21164173261 71.

Kovacs, G.G., Budka, H., 2008. Prion diseases: from protein to cell pathology. Am. J. Pathol. 172 (3), 555–565. http://dx.doi.org/10.2353/ajpath.2008.07044218245809.

Krasnianski, A., Meissner, B., Schulz-Schaeffer, W., Kallenberg, K., Bartl, M., Heinemann, U., et al., 2006. Clinical features and diagnosis of the MM2 cortical subtype of sporadic Creutzfeldt–Jakob disease. Arch. Neurol. 63 (6), 876–880. http://dx.doi.org/10.1001/archneur.63.6.876.

Lasič, S., Nilsson, M., Lätt, J., Ståhlberg, F., Topgaard, D., 2011. Apparent exchange rate mapping with diffusion MRI. Magn. Reson. Med. 66 (2), 356–365. http://dx.doi.org/10.1002/mrm.22782.

Lin, Y.R., Young, G.S., Chen, N.K., Dillon, W.P., Wong, S., 2006. Creutzfeldt–Jakob disease involvement of rolandic cortex: a quantitative apparent diffusion coefficient evaluation. A.J.N.R. Am. J. Neuroradiol. 27 (8), 1755–175916971630.

Lodi, R., Parchi, P., Tonon, C., Manners, D., Capellari, S., Strammiello, R., et al., 2009. Magnetic resonance diagnostic markers in clinically sporadic prion disease: a combined brain magnetic resonance imaging and spectroscopy study. Brain 132 (10), 2669–2679. http://dx.doi.org/10.1093/brain/awp21019755520.

Manners, D.N., Parchi, P., Tonon, C., Capellari, S., Strammiello, R., Testa, C., et al., 2009. Pathologic correlates of diffusion MRI changes in Creutzfeldt–Jakob disease. Neurology 72 (16), 1425–1431. http://dx.doi.org/10.1212/WNL.0b013e3181a1884619380702.

Marquardt, D.W., 1963. An algorithm for least-squares estimation of nonlinear parameters. J. Soc. Ind. Appl. Math. 11 (2), 431–441. http://dx.doi.org/10.1137/0111030.

Mori, S., Barker, P.B., 1999. Diffusion magnetic resonance imaging: its principle and applications. Anat. Rec. 257 (3), 102–109. http://dx.doi.org/10.1002/(SICI)1097-0185(19990615)257:3<102::AID-AR7>3.0.CO;2-610397783.

Mulkern, R.V., Vajapeyam, S., Robertson, R.L., Caruso, P.A., Rivkin, M.J., Maier, S.E., 2001. Biexponential apparent diffusion coefficient parametrization in adult vs newborn brain. Magn. Reson. Imaging 19 (5), 659–668. http://dx.doi.org/10.1016/S0730-725X(01)00383-611672624.

Murday, J.S., Cotts, R.M., 1968. Self-diffusion coefficient of liquid lithium. J. Chem. Phys. 48 (11), 4938–4945. http://dx.doi.org/10.1063/1.1668160.

Niendorf, T., Dijkhuizen, R.M., Norris, D.G., van Lookeren Campagne, M., Nicolay, K., 1996. Biexponential diffusion attenuation in various states of brain tissue: implications for diffusion-weighted imaging. Magn. Reson. Med. 36 (6), 847–857. http://dx.doi.org/10.1002/mrm.19103606078946350.

Panagiotaki, E., Schneider, T., Siow, B., Hall, M.G., Lythgoe, M.F., Alexander, D.C., 2012. Compartment models of the diffusion MR signal in brain white matter: a taxonomy and comparison. Neuroimage 59 (3), 2241–2254. http://dx.doi.org/10.1016/j.neuroimage.2011.09.081.

Parchi, P., Capellari, S., Chin, S., Schwarz, H.B., Schecter, N.P., Butts, J.D., et al., 1999. A subtype of sporadic prion disease mimicking fatal familial insomnia. Neurol. 52 (9), 1757–1763. http://dx.doi.org/10.1212/WNL.52.9.1757.

Parchi, P., de Boni, L., Saverioni, D., Cohen, M.L., Ferrer, I., Gambetti, P., et al., 2012. Consensus classification of human prion disease histotypes allows reliable identification of molecular subtypes: an inter-rater study among surveillance centres in Europe and USA. Acta Neuropathol. 124 (4), 517–529. http://dx.doi.org/10.1007/s00401-012-1002-8.

Puoti, G., Bizzi, A., Forloni, G., Safar, J.G., Tagliavini, F., Gambetti, P., 2012. Sporadic human prion diseases: molecular insights and diagnosis. Lancet Neurol. 11 (7), 618–628. http://dx.doi.org/10.1016/S1474-4422(12)70063-7.

Reese, T.G., Heid, O., Weisskoff, R.M., Wedeen, V.J., 2003. Reduction of eddy-current-induced distortion in diffusion MRI using a twice-refocused spin echo. Magn. Reson. Med. 49 (1), 177–182. http://dx.doi.org/10.1002/mrm.10308.

Riva-Amarante, E., Jiménez-Huete, A., Toledano, R., Calero, M., Alvarez-Linera, J., Escribano, J., et al., 2011. Usefulness of high b-value diffusion-weighted MRI in the diagnosis of Creutzfeldt–Jakob disease. Neurología (English Edition) 26 (6), 331–336. http://dx.doi.org/10.1016/S2173-5808(11)70078-5.

Russmann, H., Vingerhoets, F., Miklossy, J., Maeder, P., Glatzel, M., Aguzzi, A., et al., 2005. Sporadic Creutzfeldt–Jakob disease. J. Neurol. 252 (3), 338–342. http://dx.doi.org/10.1007/s00415-005-0648-8.

Satoh, K., Shirabe, S., Tsujino, A., Eguchi, H., Motomura, M., Honda, H., et al., 2007. Total Tau protein in cerebrospinal fluid and diffusion-weighted MRI as an early diagnostic marker for Creutzfeldt–Jakob disease. Dement. Geriatr. Cogn. Disord. 24 (3), 207–212. http://dx.doi.org/10.1159/000107082.

Schwarz, G., 1978. Estimating the dimension of a model. Ann. Statist. 6 (2), 461–464. http://dx.doi.org/10.1214/aos/1176344136.

Shiga, Y., Miyazawa, K., Sato, S., Fukushima, R., Shibuya, S., Sato, Y., et al., 2004. Diffusion-weighted MRI abnormalities as an early diagnostic marker for Creutzfeldt–Jakob disease. Neurol. 63 (3), 443–449. http://dx.doi.org/10.1212/01.WNL.0000134555.59460.5D.

Sijbers, J., den Dekker, A.J., Raman, E., Van Dyck, D., 1999. Parameter estimation from magnitude MR images. Int. J. Imaging Syst. Technol. 10 (2), 109–114. http://dx.doi.org/10.1002/(SICI)1098-1098(1999)10:2<109::AID-IMA2>3.0.CO;2-R.

Tschampa, H.J., Mürtz, P., Flacke, S., Paus, S., Schild, H.H., Urbach, H., 2003. Thalamic involvement in sporadic Creutzfeldt–Jakob disease: a diffusion-weighted MR imaging study. A.J.N.R. Am. J. Neuroradiol. 24 (5), 908–915.

Vitali, P., Maccagnano, E., Caverzasi, E., Henry, R.G., Haman, A., Torres-Chae, C., et al., 2011. Diffusion-weighted MRI hyperintensity patterns differentiate CJD from other rapid dementias. Neurology 76 (20), 1711–1719. http://dx.doi.org/10.1212/WNL.0b013e31821a4439.

Young, G.S., Geschwind, M.D., Fischbein, N.J., Martindale, J.L., Henry, R.G., Liu, S., et al., 2005. Diffusion-weighted and fluid-attenuated inversion recovery imaging in

Creutzfeldt–Jakob disease: high sensitivity and specificity for diagnosis. A.J.N.R. Am. J. Neuroradiol. 26 (6), 1551–1562.
Zerr, I., Kallenberg, K., Summers, D.M., Romero, C., Taratuto, A., Heinemann, U., et al., 2009. Updated clinical diagnostic criteria for sporadic Creutzfeldt–Jakob disease. Brain 132 (10), 2659–2968. http://dx.doi.org/10.1093/brain/awp191.
Zhang, H., Schneider, T., Wheeler-Kingshott, C.A., Alexander, D.C., 2012. NODDI: practical in vivo neurite orientation dispersion and density imaging of the human brain. Neuroimage 61 (4), 1000–1016. http://dx.doi.org/10.1016/j.neuroimage.2012.03.072.